

Cite this: *J. Mater. Chem. B*, 2015,  
3, 5040

## 3D conducting polymer platforms for electrical control of protein conformation and cellular functions†

Alwin Ming-Doug Wan,<sup>‡,ab</sup> Sahika Inal,<sup>‡,c</sup> Tiffany Williams,<sup>a</sup> Karin Wang,<sup>ab</sup> Pierre Leleux,<sup>cd</sup> Luis Estevez,<sup>a</sup> Emmanuel P. Giannelis,<sup>a</sup> Claudia Fischbach,<sup>b</sup> George G. Malliaras<sup>\*c</sup> and Delphine Gourdon<sup>\*ab</sup>

We report the fabrication of three dimensional (3D) macroporous scaffolds made from poly(3,4-ethylenedioxythiophene):poly(styrenesulfonate) (PEDOT:PSS) via an ice-templating method. The scaffolds offer tunable pore size and morphology, and are electrochemically active. When a potential is applied to the scaffolds, reversible changes take place in their electrical doping state, which in turn enables precise control over the conformation of adsorbed proteins (e.g., fibronectin). Additionally, the scaffolds support the growth of mouse fibroblasts (3T3-L1) for 7 days, and are able to electrically control cell adhesion and pro-angiogenic capability. These 3D matrix-mimicking platforms offer precise control of protein conformation and major cell functions, over large volumes and long cell culture times. As such, they represent a new tool for biological research with many potential applications in bioelectronics, tissue engineering, and regenerative medicine.

Received 28th February 2015,  
Accepted 2nd April 2015

DOI: 10.1039/c5tb00390c

www.rsc.org/MaterialsB

## Introduction

Ever since the first demonstration that cells could be grown on petri dishes and other planar substrates in the laboratory, the quest to better mimic the complexity of living systems with *in vitro* platforms has remained a long-standing challenge. This has been motivated by many reports that have shown radical differences between the cellular activities observed in two dimensional (2D) and three dimensional (3D) systems, due to the more complex microenvironmental conditions inherent in three dimensions.<sup>1</sup> Considering the oftentimes limited physiological relevance of 2D cell culture experiments, significant effort was subsequently devoted to the development of materials and platforms that could more accurately recreate the *in vivo* cellular microenvironment, and support 3D cell cultures *in vitro*.<sup>2</sup>

One such class of materials is conducting polymers, which appear promising due to their compliant mechanical properties, excellent compatibility with biological systems, mixed electrical and ionic conductivity,<sup>3</sup> and their ability to form 3D porous structures.<sup>4</sup> Such 3D porous scaffolds, thus, combine large solid-state surface areas with electro-physical properties that are relevant to both organic electronics and biology. In addition to the 3D structural support that such a scaffold provides, its electrical conductivity is a key property for the local delivery of applied electrical stimuli, and for the subsequent regulation of cell behavior, including adhesion, migration, and secretion. Therefore, conducting polymers have broad potential in many biological applications, including tissue engineering, diagnostics, actuation, and drug delivery systems.<sup>5</sup>

Poly(3,4-ethylenedioxythiophene):poly(styrenesulfonate) (PEDOT:PSS) is a water soluble conjugated polymer that is easily processed, and possesses metal-like conductivity, high transparency in the visible spectrum, mechanical flexibility, and good long-term stability.<sup>6</sup> Moreover, the cyto-compatibility of PEDOT:PSS has enabled its use in various *in vivo* and *in vitro* platforms.<sup>7,8</sup> In particular, previous reports showed that 2D thin films of PEDOT:tosylate, a similar conducting polymer, could electrochemically control protein conformation,<sup>9</sup> and cell secretions.<sup>10</sup> In recent years, several different strategies have been employed to develop porous PEDOT-based materials for applications in sensing, power supply, capacitance, and electrical storage.<sup>11</sup> These strategies include physical crosslinking of PEDOT:PSS particles

<sup>a</sup> Department of Materials Science and Engineering, Cornell University, Ithaca, NY 14853, USA. E-mail: dg434@cornell.edu; Fax: +1 (607) 255 2365; Tel: +1 (607) 255 1623

<sup>b</sup> Department of Biomedical Engineering, Cornell University, Ithaca, NY 14853, USA

<sup>c</sup> Department of Bioelectronics, Ecole Nationale Supérieure des Mines, CMP-EMSE, MOC, Gardanne 13541, France. E-mail: malliaras@emse.fr; Tel: +33 (0)4 42 61 66 44

<sup>d</sup> MicroVitaie Technologies, Pôle d'Activité Y. Morandat, 1480 rue d'Arménie, Gardanne 13120, France

† Electronic supplementary information (ESI) available. See DOI: 10.1039/c5tb00390c

‡ Contributed equally.

with multivalent cations,<sup>12</sup> and oxidative chemical polymerization of the EDOT monomer with non-covalent,<sup>13</sup> or ionic crosslinkers,<sup>14</sup> which can be performed within polymeric bicontinuous microemulsion-derived templates.<sup>11</sup> Additionally, Zhang and coworkers utilized post-processing techniques to prepare porous PEDOT:PSS cryogels.<sup>15</sup> Through ice-templating, the authors reported the preparation of various macroporous architectures. The technique involved crystallization of water followed by controlled sublimation of the ice by freeze drying. Following this work, Shahini and coworkers reported porous composites based on PEDOT:PSS, gelatin, and glass nanoparticles that were used to host adult human mesenchymal stem cells.<sup>16</sup> In fact, by creating porosity in the PEDOT:PSS structure, an electrically active network can be constructed, serving as a 3D template for protein adsorption, and hence as an extracellular matrix-mimicking platform to host a variety of cells. Such platforms would provide a unique tool to control and understand 3D cell-matrix interactions by varying the properties of the polymeric scaffold (*e.g.*, conductivity, surface energy, charge, local pH) *via* electrochemical stimulation.<sup>17</sup>

In this work, we report macroporous conducting PEDOT:PSS scaffolds prepared *via* an ice-templating method, that are capable of supporting 3D cell cultures. Oxidation/reduction of the electrochemically-active PEDOT:PSS scaffolds prior to cell-seeding allowed control over the adhesion and pro-angiogenic secretions of mouse fibroblasts (3T3-L1) cultured therein. Cells in oxidized scaffolds (compared to those in reduced scaffolds)

adhered in greater numbers (by 1.5 fold), while secreting significantly lower amounts of pro-angiogenic factors. Furthermore, the 3D porous PEDOT:PSS scaffolds exhibited both excellent electrochemical switching behavior, which enabled their use as the active channel of an organic electrochemical transistor (OECT), and significantly lower impedance compared to non-porous films with equal volume. Hence, macroporous PEDOT:PSS scaffolds hold promise both as extracellular matrix-mimicking structures for cell culture, as well as high-performance electrochemical devices for diagnostic and signaling applications. Combined, these capabilities represent a versatile and powerful new platform that may pave the way toward the development of many useful tools for biomedical research.

## Results and discussion

### Fabrication of 3D PEDOT:PSS platforms

Ice-templating exploits freezing of a solution with subsequent confinement of solute particles in the regions between dendrites of solvent crystals (Fig. 1A). As the ice is removed through sublimation, a 3D network of macropores is formed in the spaces that were once occupied by the solvent crystals.<sup>18,19</sup> The simplicity of ice-templating has allowed it to be employed for the preparation of a wide range of porous materials based on ceramics,<sup>20</sup> clays,<sup>21</sup> and polymers such as poly(vinyl alcohol), chitosan, gelatin, collagen, PEDOT:PSS, and Nafion<sup>®</sup>.<sup>15,16,19,22–24</sup>



**Fig. 1** (A) Schematic showing the ice templating process. (B) Photograph of PEDOT:PSS scaffolds made from molds of various shapes. Rectangular scaffolds were used in this work. (C) Low magnification SEM image of a PEDOT:PSS scaffold prepared in a PTFE mold from 1.25 wt% PEDOT:PSS dispersion with 3 wt% GOPS at a controlled freezing rate. (D) Higher magnification SEM image of a PEDOT:PSS scaffold, showing the macroporous architecture generated by ice-templating.

The technique, when combined with other removable templates, can generate porosity at multiple length scales in a single processing step.<sup>25</sup> A number of parameters (*e.g.*, composition of the solution, freezing rate, material and shape of the mold) influence the final architecture and stability of such ice-templated (or *freeze-casted*) materials.<sup>23,26</sup> Indeed, the process is highly versatile as evidenced by the multiple structures and morphologies reported by various researchers, which include lamellar microstructures, “fish-bone” morphologies, partially-oriented microwires, aligned tubular structures, and cellular materials with faceted pores.<sup>18,24,27</sup> Fig. 1B shows examples of 3D scaffolds of PEDOT:PSS prepared *via* the ice-templating method. The scaffolds are prepared by freezing an aqueous dispersion of PEDOT:PSS (with an added crosslinker) in rectangular Teflon molds ( $10 \times 7 \times 2 \text{ mm}^3$ ) at a controlled rate of  $-0.9 \text{ }^\circ\text{C min}^{-1}$  followed by sublimation of the ice phase. This process yielded highly porous macroscopic PEDOT:PSS scaffolds with controlled morphology that were suitable for use in cell-based experiments. We found that pore size could be tuned from 30 to 100  $\mu\text{m}$  by varying the freezing rate, the amount of crosslinker, and the concentration (wt%) of PEDOT:PSS. Overall, increasing any of these quantities (in isolation, or in combination) led to smaller pore sizes in the resulting scaffolds.

### Morphological and mechanical characterization

The PEDOT:PSS scaffolds that were prepared in this work *via* ice-templating exhibit a typical total pore area of  $2.2 \pm 0.1 \text{ m}^2 \text{ g}^{-1}$ , and a median pore diameter of  $39.1 \pm 2.7 \text{ }\mu\text{m}$ , as measured by mercury porosimetry (Fig. S1, ESI†). The elastic modulus measured in an aqueous environment is  $4.5 \pm 0.6 \text{ kPa}$ , indicating a good stiffness match with a variety of tissues *in vivo* (Fig. S2, ESI†). The detailed morphology and macroporous structure of the scaffolds can be seen by SEM (Fig. 1C and D), which clearly reveals an interconnected network of open macropores that should enable efficient cell invasion and mass transport. While immersing the scaffolds in an aqueous environment certainly causes some swelling of the polymer, the presence of the crosslinker aids substantially in preserving the structure of the scaffolds. Indeed, SEM images of scaffolds that were soaked in cell culture media for several days showed that their microstructure remained unchanged from as-fabricated scaffolds.

### Electrical characterization

In order to characterize the electrical activity of our porous scaffolds, we fabricated organic electrochemical transistors (OECTs) wherein a PEDOT:PSS scaffold comprised the active channel of the transistor. OECTs based on thin PEDOT:PSS films have recently been used as drug screening platforms,<sup>28</sup> for monitoring cell attachment and coverage,<sup>29</sup> for electrophysiological recordings of *in vivo* brain activity or electrocardiograms,<sup>7,30</sup> and for assessing tissue dysfunction upon exposure to toxins,<sup>31</sup> or pathogens.<sup>32</sup> A schematic demonstrating the layout of these OECTs and a photograph of typical devices are given in Fig. 2A. The scaffold is patterned between two Au contacts that act as the source and the drain electrodes, while a second scaffold is used as the gate electrode. In this configuration, where the

entire scaffold is submerged in an electrolyte, its conductivity decreases by the injection of cations, triggered by a positive bias ( $V_G$ ) applied through the other scaffold, which acts as the gate electrode. The change in the drain current ( $I_D$ ) upon application of a gate pulse of 0.6 V is shown in Fig. 2B. Due to the large size of the channel, the switching speed of the OECT exceeds 1 s; however, the current–time profile shows that the current recovers to its initial value upon removal of the voltage pulse at the gate. The transfer characteristics of these porous transistors were evaluated from a series of  $V_G$  steps while monitoring the drain current at constant drain voltage ( $V_D = -0.6 \text{ V}$ ). Fig. 2C shows that maximum transconductance reaches  $0.72 \pm 0.05 \text{ mS}$  at a gate bias of 0 V and a drain voltage of  $-0.6 \text{ V}$ . This performance is comparable to OECTs comprised of a spin-cast thin film of PEDOT:PSS. Due to the structural inhomogeneity within the scaffolds, the performance of the transistors differs; nevertheless, modulation of the current in the channel is always observed when a gate bias is applied.

Electrical impedance is a key property that affects the quality of recording devices, and conducting polymers have been shown to reduce the impedance of classical electrodes, enabling recordings with higher signal-to-noise ratio.<sup>33</sup> The porous morphology of the scaffolds allows for a significantly higher surface-to-volume ratio, resulting in low impedance that is promising for neural probe applications (Fig. S3, ESI†). The lower impedance of the 3D architecture can be attributed to an increased ability of ions to penetrate into the conducting polymer network. We note that electrochemical switching is not expected to significantly alter the microstructure of the PEDOT:PSS scaffolds. In fact, Aasmundtveit and coworkers showed with *in situ* grazing incidence diffraction techniques that oxidation of PEDOT doped with *p*-toluenesulfonate had no effect on the arrangement of the polymer chains, and only slightly (and reversibly) decreased the structural order.<sup>34</sup> Overall, these results demonstrate the feasibility of employing porous PEDOT:PSS scaffolds in bioelectronics devices, paving the way toward *in vitro* tissue models based on conducting scaffolds that possess dynamic monitoring and control capabilities.

### Cell invasion and matrix deposition

To evaluate the use of PEDOT:PSS scaffolds for cell culture experiments, we seeded them with 3T3-L1 mouse preadipocyte cells (representative of stromal cells). Briefly, the scaffolds were individually placed into the wells of a 12-well plate, and cells were pipetted onto the top of the scaffolds in  $\alpha$ MEM media containing 33 vol% matrigel to promote adhesion. The scaffolds were incubated for 30 minutes to allow the cells to adhere, after which fresh media was added to the wells. The scaffolds were then cultured dynamically on an orbital shaker to promote cell survival and growth *via* convective mass transfer.

The scaffold-bound cell populations were typically characterized after 24 hours of culture (with the exception of long-term viability studies). The interior of chemically-fixed (crosslinked) scaffolds were revealed by cryo-ultramicrotome sectioning, and subsequent SEM images indicated that 3T3-L1s successfully invaded the scaffold and adhered to the 3D PEDOT:PSS architectures (Fig. 3A).



Fig. 2 (A) 3D, cross sectional, and top view schematics of the OECT structure where  $W = 6$  mm and  $L = 6$  mm (figure not to scale). The photograph at right shows typical OECTs. The conductivity of the PEDOT:PSS scaffold interfacing the source and drain electrodes decreases by the injection of cations from the electrolyte, triggered by an applied bias through the second scaffold which acts as the gate electrode. (B) Transient characteristics of a transistor ( $W = 6$  mm,  $L = 6$  mm,  $d = 2$  mm) prepared from a porous scaffold. The length of the pulse at the gate electrode ( $V_G = 0.6$  V) was 6 s.  $V_D$  was constant at  $-0.6$  V. (C) Transfer characteristics of an OECT comprised of a porous scaffold, and corresponding transconductance values at  $V_D = -0.6$  V.

Further, a fluorescent viability assay of unfixed scaffolds showed that the majority of the cells were viable after both short-term (24 hours) and long-term (7 days) culture (Fig. 3B). To assess whether the 3T3-L1s were performing regular cell functions, such as the assembly of an extracellular matrix (ECM), we utilized fluorescent immunostaining to visualize cell-deposited fibronectin (Fn) fibers. Indeed, Fn not only decorated the surfaces of the scaffold, but was also assembled into thin fibers around the periphery of cells (Fig. 3C), indicating the ability of the cells to polymerize soluble Fn into fibers. Further SEM imaging after scaffold decellularization showed clearly visible protein fibers across the porous structure (Fig. 3D). Interestingly, SEM-detectable fibers had larger diameters than fibers detected by immunofluorescence, suggesting that they may be composed of collagen (another major ECM protein), rather than Fn. Collectively, these results indicate that the 3T3-L1 cells not only adhered to the scaffolds, but also performed regular cell functions, such as ECM deposition and remodeling. These findings suggest that PEDOT:PSS scaffolds provide a suitable 3D environment for fibroblasts to attach, grow, and function normally, which represent essential criteria for the development of a physiologically relevant 3D cell-culture platform based on PEDOT:PSS. Indeed, Shahini and coworkers recently showed that increasing the concentration of PEDOT:PSS in a porous composite scaffold used to culture mesenchymal stem cells enhanced the viability of the stem cells, which the authors attributed to the improved microstructure of

the scaffold, or enhanced electrical signaling between cells.<sup>16</sup> Similarly, the high level of activity exhibited by the 3T3-L1 cells in our PEDOT:PSS scaffolds might stem from improved intracellular electrical signaling, due to the high conductivity of the polymer.

### Control of fibronectin conformation

While the porous 3D form of PEDOT:PSS represents an excellent scaffold material to support cell culture, the scaffolds also exhibit electrical properties comparable to their 2D thin-film analogs (Fig. S3, ESI†). The electrochemical properties of PEDOT:PSS can be reversibly manipulated by changing its redox state, and conducting polymers (including PEDOT:PSS) have previously been used to alter the behavior of adhered cells,<sup>17,35,36</sup> and of adsorbed proteins.<sup>9</sup> Thus, we examined whether the redox state of the 3D scaffold could be used to control the conformation of adsorbed Fn, which further affects the adhesion of cells and their subsequent secretion behavior. To this end, we assessed Fn conformation with intramolecular Förster Resonance Energy Transfer (FRET) imaging, using trace amounts of Fn molecules that were dual-labeled for FRET, as previously described.<sup>9,37</sup> A bipolar power supply sourced an oxidizing potential of +1 V to one scaffold, and a reducing potential of  $-1$  V to another, while the scaffolds were both submerged in electrically-grounded cell culture media, containing  $100 \mu\text{g mL}^{-1}$  of added fibronectin (of which only 10% was labeled for FRET, to avoid spurious intermolecular FRET). The bias was



Fig. 3 (A) SEM micrograph of PEDOT:PSS scaffold after 24 hours of cell culture, showing invasion of the scaffold by 3T3-L1s. (B) Fluorescence micrograph of a PEDOT:PSS scaffold after 7 days of 3T3-L1 culture, showing very high cell viability. Live cells are stained with calcein (green), and dead cells are stained with propidium iodide (red). The pores of the scaffold are visible as large circular dark regions. (C) Fluorescence micrograph of a PEDOT:PSS scaffold, with cell-deposited fibronectin fibers (green) after 24 hours of 3T3-L1 culture. Cell nuclei are stained with DAPI (blue). (D) SEM image of a decellularized scaffold, clearly showing protein fibers produced by 3T3-L1 cells during 24 hours of culture.

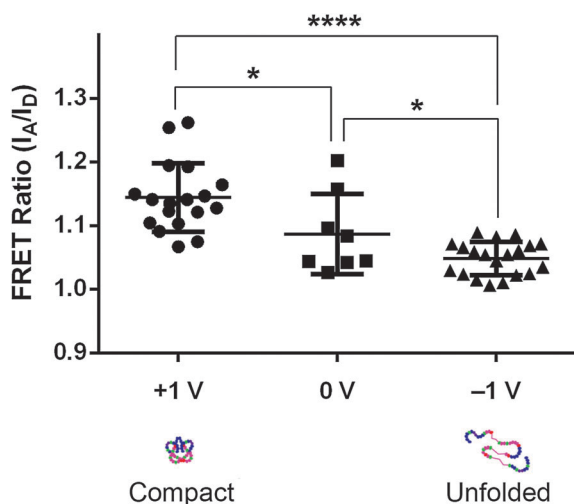


Fig. 4 Measured FRET intensity ratio for scaffold-adsorbed Fn, on oxidized ( $1.14 \pm 0.23$ ), neutral ( $1.09 \pm 0.18$ ), and reduced ( $1.05 \pm 0.11$ ) PEDOT:PSS scaffolds. Fn on oxidized scaffolds exhibits FRET ratios that are 10% higher than those observed on reduced scaffolds, indicating more compact Fn conformations in the oxidized state, and more unfolded Fn conformations in the reduced state (as illustrated by the schematics at bottom). In all cases, \* indicates  $p < 0.05$ , and \*\*\*\* indicates  $p < 0.0001$ . Bars show means and standard deviations, with 8 to 20 measurements per condition.

maintained for 1 hour at 37 °C, after which the scaffolds were rinsed thoroughly in PBS, and imaged on a confocal microscope.

Our FRET data (combined with the FRET intensity ratio calibration shown in Fig. S4, ESI†) indicate that the conformation of scaffold-adsorbed Fn varies as a function of redox potential, with Fn molecules assuming more compact conformations (high FRET ratios) in the oxidized scaffolds, and more extended conformations (low FRET ratios) in the reduced scaffolds (Fig. 4). These findings are in agreement with previous results on 2D thin films of PEDOT:tosylate, a similar conducting polymer, where Fn conformation followed the same trend.<sup>9</sup> We chose our potentials (+1 V and -1 V) to be small enough to avoid hydrolysis of water above 1.23 V and over-oxidation of the polymer, but also large enough to achieve complete electrochemical switching of PEDOT:PSS,<sup>38</sup> and enable presentation of the full range of available Fn molecular conformations.<sup>9</sup>

#### Control of cell adhesion and pro-angiogenic capability

Given the importance of Fn conformation in guiding numerous cell functions, as well as previous reports that the redox state of polymer surfaces affects cell adhesion,<sup>35,36</sup> we investigated whether altering the redox state of PEDOT:PSS scaffolds would affect the adhesion and the pro-angiogenic secretion of cells seeded therein. Pairs of scaffolds were biased at oxidizing and reducing potentials of +1 V and -1 V (as described above for the FRET experiment), and subsequently, 3T3-L1 cells were seeded into the scaffolds (as described above for the cell culture experiments in unbiased scaffolds). Cell culture took place in

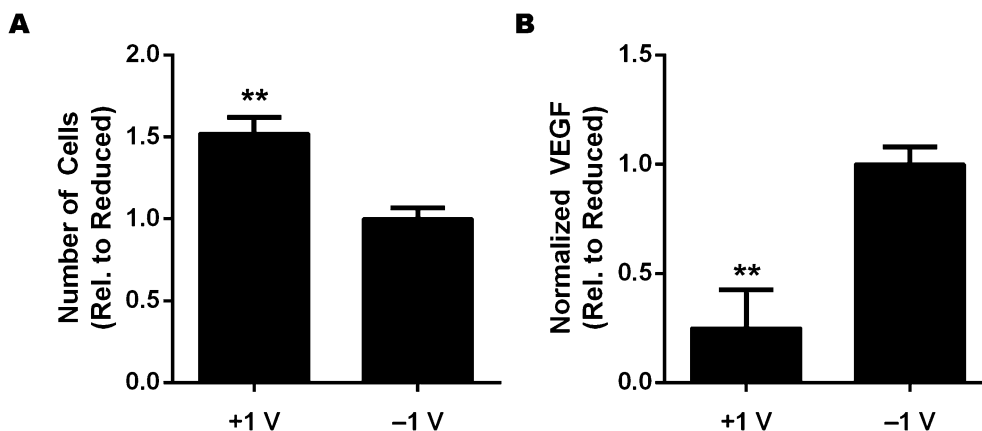


Fig. 5 (A) Relative number of 3T3-L1 cells adhered to oxidized (+1 V) and reduced (−1 V) PEDOT:PSS scaffolds, quantified by fluorometric DNA assay. Cells adhere in significantly higher numbers (50% more) to oxidized scaffolds as compared to reduced scaffolds. (B) Relative levels of vascular endothelial growth factor (VEGF) secreted by 3T3-L1s (normalized to cell number) cultured in oxidized and reduced scaffolds over 24 hours. Cells in reduced scaffolds secrete 4 times more VEGF as compared to those in oxidized scaffolds. In all cases, \*\* indicates  $p < 0.01$ .

the absence of applied bias, and after 24 hours, the total number of cells present in the scaffolds was quantified with a fluorometric DNA assay. The results show that 50% more cells adhered to the oxidized scaffolds as compared to the reduced scaffolds (Fig. 5A), indicating a redox-dependent modulation of cell adhesion that is in agreement with previous findings.<sup>36</sup> Importantly, cell proliferation did not differ significantly in the first 24 hours, implying that the observed difference in cell number is indeed due to adhesion.

Altered Fn conformation occurs *in vivo*, and in particular, in the context of cancer. Chandler and coworkers recently showed that the *in vivo* tumor microenvironment is characterized by more extended/unfolded Fn fibers than are found in healthy tissue.<sup>39</sup> Moreover, this tumor-associated partial unfolding of Fn has been implicated in the enhanced secretion of pro-angiogenic factors by adipogenic precursor cells, suggesting a link to tumor angiogenesis.<sup>10</sup> Since our experiments showed that we could alter Fn conformation by manipulating the redox state of the PEDOT:PSS scaffolds, we sought to assess whether this could affect the pro-angiogenic capability of 3T3-L1 cells cultured in oxidized and reduced scaffolds. We cultured 3T3-L1s in oxidized and reduced scaffolds, as described above, and after 24 hours, we collected the media from the wells in which the scaffolds were cultured. To quantify pro-angiogenic potential, we measured the concentration of vascular endothelial growth factor (VEGF) present in the media using ELISA (normalized to the number of cells, as measured by DNA assay), and found that the cells cultured in reduced scaffolds secreted 4 times more VEGF than those cultured in oxidized scaffolds (Fig. 5B). Previous studies using both Fn molecular films<sup>10</sup> and thin Fn fibrillar networks<sup>40</sup> have shown that altered Fn conformation controls adhesion and pro-angiogenic behaviors *via* an integrin-switching mechanism (in particular, the preferential engagement of  $\alpha_v\beta_3$  rather than  $\alpha_5\beta_1$  integrins in the presence of unfolded Fn); however, further studies are required to determine if the voltage-induced alterations of Fn conformation are similarly responsible for the observed cell behavior in our PEDOT:PSS scaffolds. Nonetheless, these results suggest that the reduced Fn-coated scaffolds mimic to some

degree the conformation of tumor-associated Fn fibers (as measured by FRET), which enhance the pro-angiogenic capability of adipogenic precursors. Interestingly, we note that the difference in VEGF secretion observed between the two redox states in the 3D PEDOT:PSS scaffolds is significantly enhanced when compared to previous results obtained with a 2D thin film system.<sup>10</sup> This difference points toward the importance of physiologically-relevant 3D cell culture systems, which can perhaps more fully capture the *in vivo* magnitude of cell responses that might otherwise be muted in 2D cell culture systems.

## Conclusions

In this work we demonstrated that PEDOT:PSS can be templated into 3D macroporous architectures that provide an electrically conductive, low-impedance, and biocompatible scaffold that supports fibroblast culture. 3T3-L1s were successfully seeded into the scaffolds and remained viable for 7 days, while performing regular cell functions such as adhesion and deposition of ECM components. Additionally, electrochemical stimulation of the scaffolds (prior to cell seeding) enabled control over the conformation of adsorbed ECM proteins such as fibronectin, subsequently modulating the adhesion and pro-angiogenic secretion of 3T3-L1s cultured in those scaffolds. Our results indicate that cells adhered in greater numbers (50% more) onto oxidized scaffolds coated with compact Fn than onto reduced scaffolds coated with unfolded Fn, while they secreted 4 times more VEGF in reduced scaffolds than in oxidized scaffolds. These trends recapitulate the redox-dependent cell adhesion and pro-angiogenic capability observed in 2D thin-film conducting polymer systems, but appear to be enhanced in 3D (particularly in the case of secretions). Finally, we demonstrated that PEDOT:PSS scaffolds form low impedance electrodes and can be integrated as the active channel in OECTs, yielding high-performance devices suitable for sensing, and with the potential to detect real-time signals from cells cultured within the scaffolds. Together, our findings indicate that macroporous conducting polymer scaffolds

represent a powerful new platform that can not only control protein conformation and various cell functions, but also simultaneously operate as the active component of a transistor. In this context, such scaffolds will potentially pave the way toward electrically-active, physiologically-relevant 3D tissue-culture platforms that can control and monitor cell functions in changing microenvironments.

## Experimental

### Scaffold preparation

Scaffolds were fabricated from an aqueous dispersion of PEDOT:PSS (Clevios PH-1000, Heraeus) at a concentration of 1.25 wt%, with 3-glycidioxypropyltrimethoxysilane (GOPS) (Sigma-Aldrich) added as a crosslinker at 3 wt% to improve mechanical robustness and stability in water. The PEDOT:PSS/GOPS dispersion was poured into rectangular Teflon molds,  $10 \times 7 \times 2 \text{ mm}^3$  in size. The samples were then placed in a freeze-dryer (VirTis Advantage Plus ES; SP Scientific; PA, USA), where they were frozen from  $5^\circ\text{C}$  to  $-40^\circ\text{C}$  at a controlled rate of  $-0.9^\circ\text{C min}^{-1}$ , at which point the ice phase was sublimed from the scaffolds. Following sublimation, the scaffolds were baked at  $140^\circ\text{C}$  for one hour.

### Scaffold characterization

Scaffold microstructure was characterized using scanning electron microscopy (SEM), mercury intrusion porosimetry, and polarized optical microscopy. In addition, SEM (Leica 440; Leica Microsystems; Wetzlar, Germany) was used to assess and visualize the infiltration of cells into the scaffolds. Cell seeded-scaffolds were rinsed in PBS to remove excess formaldehyde used for chemical fixation of cells. The scaffolds were then placed in a freeze-dryer to remove the water. The scaffolds then underwent cryo-ultramicrotomy (Leica EM FC7; Leica Microsystems; Wetzlar, Germany) at a shallow angle relative to the top face in order to expose a range of depths for SEM imaging. Prior to imaging, the samples were sputtered with a thin layer of Au/Pd to improve micrograph quality. All micrographs were obtained at 10 keV. Mercury intrusion porosimetry (Autopore IV 9500; Micromeritics; Atlanta, USA) was performed on dry monoliths to probe the size of pores produced using ice templating. Samples were placed in glass penetrometers of known volume and weight. Analyses were performed using an automated procedure where the penetrometers were first evacuated to  $50 \mu\text{m Hg}$  and then filled with mercury at 0.2 psi. The pressure applied to the sample inside the penetrometer was then ramped stepwise to 44 psi to probe pores larger than approximately  $4 \mu\text{m}$  in diameter.

Mechanical testing of scaffolds was performed using a dynamic mechanical analyzer (DMA; DMA Q800; TA Instruments; DE, USA) in which samples were placed under compressive loads. Stability tests were performed by placing samples at room-temperature in cell culture medium ( $\alpha\text{MEM}$ ) overnight. Measurements were performed at a single loading cycle, with an initial contact force of 0.05 N and loaded at a fixed force-rate of  $0.005 \text{ N min}^{-1}$  to 0.075 N. Elastic modulus was calculated as the slope of the linear part of the stress-strain curve near zero strain.

### Cell culture experiments

2 mm thick scaffolds were prepared for cell culture experiments by being soaked for 20 minutes in 70% ethanol for disinfection, and then rinsed 5 times with sterile PBS (Life Technologies). If electrochemical switching was required, a bipolar power supply sourced an oxidizing potential of +1 V to one scaffold, and a reducing potential of  $-1 \text{ V}$  to another, while the scaffolds were both submerged in electrically-grounded cell culture media. The bias was maintained for 1 hour at  $37^\circ\text{C}$ , after which the scaffolds were rinsed thoroughly in sterile PBS. Cell adhesion was assessed with 3T3-L1 cells (ATCC #CL-173), an adipogenic subtype of mouse fibroblasts. These cells were incubated in  $\alpha\text{MEM}$  (Sigma-Aldrich) containing 10 vol% fetal bovine serum (FBS, Tissue Culture Biologicals) and 1 vol% penicillin/streptomycin (pen/strep) (Life Technologies) prior to seeding. The cells were seeded in  $30 \mu\text{L}$  suspensions (containing 1.5 million cells) into scaffolds and were allowed to adhere for 30 minutes. Then, fresh media was added to the wells containing the scaffolds, and they were cultured dynamically on an orbital shaker for the duration of the experiment (*i.e.*, 24 hours or 7 days), at  $37^\circ\text{C}$  (5%  $\text{CO}_2$ ). Afterward, cell-seeded scaffolds were soaked in 4% ice-cold paraformaldehyde for chemical fixation and stained with 4',6-diamidino-2-phenylindole (DAPI), calcein AM, and propidium iodide (PI) (all from Life Technologies), in order to evaluate cell viability and infiltration into the scaffolds through fluorescence microscopy. To detect cell-deposited Fn fibers, immunofluorescent staining of the scaffolds was performed with a primary antibody raised against Fn (Sigma-Aldrich), an Alexa Fluor 488-labelled secondary antibody, and DAPI (both from Life Technologies). Fluorescent microscopy was performed on a Zeiss Observer Z.1 microscope with an AxioCam MRm camera.

### Fluorometric DNA assay

To measure the number of cells in the scaffolds, the scaffolds were washed five times in PBS, and then mechanically disintegrated and sonicated (Branson Sonifier 150) in lysis buffer (25 mM Tris-HCl, 0.4 M NaCl, 0.5% SDS). Lysates were then centrifuged, and the supernatant was assayed for DNA content using PicoGreen<sup>®</sup> dsDNA Assay Kit (Life Technologies), and a fluorescence plate reader (Tecan M1000) according to manufacturer instructions.

### Fibronectin and FRET labeling

Fibronectin (Fn) was obtained from Life Technologies, NY. AlexaFluor 488 succinimidyl ester and AlexaFluor 546 maleimide (Invitrogen, CA) were used to label Fn for intramolecular FRET as previously described by Smith *et al.*<sup>37</sup> Labeling ratios and Fn concentrations were determined using a DU<sup>®</sup>730 UV/Vis spectrophotometer (Beckman, IN) at 280 nm, 495 nm, and 556 nm. Soluble calibration of FRET-labeled Fn was carried out in guanidine hydrochloride (GdnHCl) solution at concentrations of 0 M, 2 M, and 4 M to obtain FRET ratios, defined as acceptor/donor intensity ratios ( $I_A/I_D$ ), as a function of protein denaturation (Fig. S4, ESI<sup>†</sup>).

### FRET data acquisition and analysis

Fn-adsorbed scaffolds were imaged with a Zeiss 710 confocal microscope (Zeiss, Munich, Germany). 16-bit z-stack images were acquired using the C-Apochromat water-immersion 40×/1.2 objective, a pinhole of 1 AU, 488 nm laser with 30% laser power, pixel dwell time of 6.3 μs, PMT1 and PMT2 gains of 600 V, and z step size of 0.5 μm. FRET-labeled Fn was excited with a 488 nm laser line; emissions from donor and acceptor fluorophores were simultaneously collected in the PMT1 channel (514–526 nm) and the PMT2 channel (566–578 nm), respectively. These z-stack images were analyzed with customized Matlab code to generate FRET ratio ( $I_A/I_D$ ) images (data not shown) as well as mean FRET ratios (Fig. 4) for all z-slices in a z-stack.

### VEGF quantification

To analyze VEGF secretions after 24 hours, media was collected from the wells in which the scaffolds were cultured, and analyzed *via* Quantikine mouse VEGF ELISA (R&D Systems). VEGF content was normalized to cell numbers as determined by fluorometric DNA assay.

### OECT fabrication

The OECT fabrication process included the deposition of metal electrodes and patterning of the PEDOT:PSS scaffold active layer. Au source and drain contacts (100 nm) were thermally evaporated on glass substrates. The porous scaffold was immobilized between the two contacts by applying a few drops of PEDOT:PSS dispersion containing 1 wt% GOPS, 5 vol% ethylene glycol, and 0.05 vol% dodecylbenzenesulfonic acid on top of the Au pads, followed by an annealing step at 110 °C for 30 min. This resulted in a transistor channel with a width ( $W$ ) of 6 mm and a length ( $L$ ) of 6 mm (Fig. 2A).

### Characterization of devices

Transistors were operated in the common source configuration. The electrolyte was an aqueous NaCl (0.1 M) solution into which the scaffolds used as the transistor channel and as the gate electrode were immersed. The  $I$ - $V$  characteristics of the OECTs were measured using a National Instruments PXIe-1062Q system. Two NIPXI-4071 digital multimeters measured drain and gate currents, and a NI-PXI 6289 measured drain and gate voltage. All of the measurements were triggered through the built-in PXI architecture. The recorded signals were saved and analyzed using customized LabVIEW software. Impedance spectra of the scaffolds and of the PEDOT:PSS films attached to Au electrodes were measured using an Autolab potentiostat equipped with an FRA module. Bulk (non-porous) PEDOT:PSS films were prepared by pouring the PEDOT:PSS/GOPS (1.25 wt% PEDOT:PSS and 3 wt% GOPS) dispersion into poly(dimethylsiloxane) (PDMS) molds attached to Au electrodes. Commercially available Ag/AgCl and Pt electrodes were used as the reference and counter electrodes, respectively. The applied voltage was 0.01 V and the electrolyte solution was aqueous NaCl (0.1 M).

### Statistical analysis

One-way ANOVA with Tukey's post test and Student's  $t$ -test were used to determine statistical significance between conditions in GraphPad Prism (GraphPad Software, California USA). In all cases,  $p < 0.05$  is indicated by a single star (\*),  $p < 0.01$  by a double star (\*\*), and  $p < 0.0001$  by four stars (\*\*\*\*).

### Acknowledgements

This work was funded by NSF under award DMR-1352299 (D.G.), the region PACA and ANR under award PolyProbe-ANR-13-BSV5-0019-01 (G.G.M.), and NIH/NCI under award R01 CA185293 (C.F. and D.G.). S.I. acknowledges Paul Molino (University of Wollongong) and Jonathan Rivnay (EMSE) for their help in electrical measurements. This research made use of the Cornell Center for Materials Research shared facilities (CCMR) supported through the NSF MRSEC program (NSF DMR-1120296). This work was also supported by the Cornell University Biotechnology Resource Center (BRC) Imaging Facility.

### References

- 1 M. A. Schwartz and C. S. Chen, *Science*, 2013, **339**, 402–404; E. Cukierman, R. Pankov, D. R. Stevens and K. M. Yamada, *Science*, 2001, **294**, 1708–1712.
- 2 F. Pampaloni, E. G. Reynaud and E. H. K. Stelzer, *Nat. Rev. Mol. Cell Biol.*, 2007, **8**, 839–845; E. Carletti, A. Motta and C. Migliaresi, in *3D Cell Culture*, ed. J. W. Haycock, Humana Press, 2011, pp. 17–39; J. M. Holzwarth and P. X. Ma, *J. Mater. Chem.*, 2011, **21**, 10243–10251.
- 3 L. H. Jimison, J. Rivnay and R. M. Owens, *Organic Electronics*, Wiley-VCH Verlag GmbH & Co. KGaA, 2013, pp. 27–67.
- 4 A. I. Cooper, *Adv. Mater.*, 2009, **21**, 1291–1295.
- 5 J. L. S. Antonio, L. M. Lira, V. R. Goncales and S. I. Cordoba de Torresi, *Electrochim. Acta*, 2013, **101**, 216–224.
- 6 S. Kirchmeyer and K. Reuter, *J. Mater. Chem.*, 2005, **15**, 2077–2088; B. Groenendaal, F. Jonas, D. Freitag, H. Pielartzik and J. Reynolds, *Adv. Mater.*, 2000, **12**, 481–494.
- 7 D. Khodagholy, T. Doublet, P. Quilichini, M. Gurfinkel, P. Leleux, A. Ghestem, E. Ismailova, T. Herve, S. Sanaur, C. Bernard and G. G. Malliaras, *Nat. Commun.*, 2013, **4**, 1575.
- 8 S. Venkatraman, J. Hendricks, Z. A. King, A. J. Sereno, S. Richardson-Burns, D. Martin and J. M. Carmena, *IEEE Trans. Neural Syst. Rehabil. Eng.*, 2011, **19**, 307–316; S. M. Richardson-Burns, J. L. Hendricks, B. Foster, L. K. Povlich, D.-H. Kim and D. C. Martin, *Biomaterials*, 2007, **28**, 1539–1552.
- 9 A. M. D. Wan, R. M. Schur, C. K. Ober, C. Fischbach, D. Gourdon and G. G. Malliaras, *Adv. Mater.*, 2012, **24**, 2501–2505.
- 10 A. M. D. Wan, E. M. Chandler, M. Madhavan, D. W. Infanger, C. K. Ober, D. Gourdon, G. G. Malliaras and C. Fischbach, *Biochim. Biophys. Acta, Gen. Subj.*, 2013, **1830**, 4314–4320.
- 11 B. H. Jones, K.-Y. Cheng, R. J. Holmes and T. P. Lodge, *Macromolecules*, 2011, **45**, 599–601.

- 12 S. Ghosh, J. Rasmusson and O. Inganäs, *Adv. Mater.*, 1998, **10**, 1097–1099.
- 13 R. Du, Y. Xu, Y. Luo, X. Zhang and J. Zhang, *Chem. Commun.*, 2011, **47**, 6287–6289.
- 14 T. Dai, X. Jiang, S. Hua, X. Wang and Y. Lu, *Chem. Commun.*, 2008, 4279–4281.
- 15 X. Zhang, C. Li and Y. Luo, *Langmuir*, 2011, **27**, 1915–1923.
- 16 M. Y. Aref Shahini, K. J. Walker, M. A. Eastman, H. Hatami-Marbini, B. J. Smith, J. L. Ricci, S. V. Madihally, D. Vashae and L. Tayebi, *Int. J. Nanomed.*, 2014, **9**, 167–181.
- 17 M. H. Bolin, K. Svennersten, D. Nilsson, A. Sawatdee, E. W. H. Jager, A. Richter-Dahlfors and M. Berggren, *Adv. Mater.*, 2009, **21**, 4379–4382.
- 18 S. Deville, E. Saiz, R. K. Nalla and A. P. Tomsia, *Science*, 2006, **311**, 515–518.
- 19 H. Zhang and A. I. Cooper, *Adv. Mater.*, 2007, **19**, 1529–1533; M. C. Gutierrez, M. L. Ferrer and F. del Monte, *Chem. Mater.*, 2008, **20**, 634–648.
- 20 S. Deville, *Adv. Eng. Mater.*, 2008, **10**, 155–169.
- 21 M. D. Gawryla, L. Liu, J. C. Grunlan and D. A. Schiraldi, *Macromol. Rapid Commun.*, 2009, **30**, 1669–1673; S. M. Alhassan, S. Qutubuddin and D. Schiraldi, *Langmuir*, 2010, **26**, 12198–12202.
- 22 L. Estevez, A. Kelarakis, Q. Gong, E. H. Da'as and E. P. Giannelis, *J. Am. Chem. Soc.*, 2011, **133**, 6122–6125; C. Arbizzani, S. Beninati, E. Manferrari, F. Soavi and M. Mastragostino, *J. Power Sources*, 2006, **161**, 826–830; L. Ren, K. Tsuru, S. Hayakawa and A. Osaka, *Biomaterials*, 2002, **23**, 4765–4773; S. V. Madihally and H. W. T. Matthew, *Biomaterials*, 1999, **20**, 1133–1142; M. C. Gutierrez, Z. Y. Garcia-Carvajal, M. Jobbagy, F. Rubio, L. Yuste, F. Rojo, M. L. Ferrer and F. del Monte, *Adv. Funct. Mater.*, 2007, **17**, 3505–3513; S. Deville, *J. Mater. Res.*, 2013, **28**, 2202–2219.
- 23 F. J. O'Brien, B. A. Harley, I. V. Yannas and L. Gibson, *Biomaterials*, 2004, **25**, 1077–1086.
- 24 H. Zhang, I. Hussain, M. Brust, M. F. Butler, S. P. Rannard and A. I. Cooper, *Nat. Mater.*, 2005, **4**, 787–793.
- 25 L. Estevez, R. Dua, N. Bhandari, A. Ramanujapuram, P. Wang and E. P. Giannelis, *Energy Environ. Sci.*, 2013, **6**, 1785–1790.
- 26 E. Munch, E. Saiz, A. P. Tomsia and S. Deville, *J. Am. Ceram. Soc.*, 2009, **92**, 1534–1539.
- 27 S. Deville, C. Viazzi, J. Leloup, A. Lasalle, C. Guizard, E. Maire, J. Adrien and L. Gremillard, *PLoS One*, 2011, **6**, e26474.
- 28 C. Yao, C. Xie, P. Lin, F. Yan, P. Huang and I. M. Hsing, *Adv. Mater.*, 2013, **25**, 6575–6580.
- 29 P. Lin, F. Yan, J. Yu, H. L. W. Chan and M. Yang, *Adv. Mater.*, 2010, **22**, 3655–3660.
- 30 A. Campana, T. Cramer, D. T. Simon, M. Berggren and F. Biscarini, *Adv. Mater.*, 2014, **26**, 3874–3878; P. Leleux, C. Johnson, X. Strakosas, J. Rivnay, T. Herve, R. M. Owens and G. G. Malliaras, *Adv. Healthcare Mater.*, 2014, **3**, 1377–1380.
- 31 S. A. Tria, L. H. Jimison, A. Hama, M. Bongo and R. M. Owens, *Biochim. Biophys. Acta, Gen. Subj.*, 2013, **1830**, 4381–4390.
- 32 S. A. Tria, M. Ramuz, M. Huerta, P. Leleux, J. Rivnay, L. H. Jimison, A. Hama, G. G. Malliaras and R. M. Owens, *Adv. Healthcare Mater.*, 2014, **3**, 1053–1060.
- 33 K. A. Ludwig, N. B. Langhals, M. D. Joseph, S. M. Richardson-Burns, J. L. Hendricks and D. R. Kipke, *J. Neural Eng.*, 2011, **8**, 014001; X. Cui, J. F. Hetke, J. A. Wiler, D. J. Anderson and D. C. Martin, *Sens. Actuators, A*, 2001, **93**, 8–18; D.-H. Kim, S. Richardson-Burns, L. Povlich, M. R. Abidian, S. Spanninga, J. Hendricks and D. C. Martin, in *Indwelling Neural Implants: Strategies for Contending with the In Vivo Environment*, ed. W. M. Reichert, CRC Press, Taylor and Francis, Boca Raton (FL), 2008, pp. 165–207.
- 34 K. E. Aasmundtveit, E. J. Samuelsen, O. Inganäs, L. A. A. Pettersson, T. Johansson and S. Ferrer, *Synth. Met.*, 2000, **113**, 93–97.
- 35 J. Y. Wong, R. Langer and D. E. Ingber, *Proc. Natl. Acad. Sci. U. S. A.*, 1994, **91**, 3201–3204; K. Svennersten, M. H. Bolin, E. W. H. Jager, M. Berggren and A. Richter-Dahlfors, *Biomaterials*, 2009, **30**, 6257–6264.
- 36 C. Salto, E. Saindon, M. Bolin, A. Kancierzewska, M. Fahlman, E. W. H. Jager, P. Tengvall, E. Arenas and M. Berggren, *Langmuir*, 2008, **24**, 14133–14138; A. M. D. Wan, D. J. Brooks, A. Gumus, C. Fischbach and G. G. Malliaras, *Chem. Commun.*, 2009, 5278–5280; A. Gumus, J. P. Califano, A. M. D. Wan, J. Huynh, C. A. Reinhart-King and G. G. Malliaras, *Soft Matter*, 2010, **6**, 5138–5142.
- 37 M. L. Smith, D. Gourdon, W. C. Little, K. E. Kubow, R. A. Eguiluz, S. Luna-Morris and V. Vogel, *PLoS Biol.*, 2007, **5**, e268.
- 38 J. C. Gustafsson, B. Liedberg and O. Inganäs, *Solid State Ionics*, 1994, **69**, 145–152.
- 39 E. M. Chandler, M. P. Saunders, C. J. Yoon, D. Gourdon and C. Fischbach, *Phys. Biol.*, 2011, **8**, 015008.
- 40 K. Wang, R. C. Andresen Eguiluz, F. Wu, B. R. Seo, C. Fischbach and D. Gourdon, *Biomaterials*, 2015, **54**, 63–71.